Chemical Engineering Journal 534 (2026) 174178

Contents lists available at ScienceDirect

Chemical Engineering Journal

journal homepage: www.elsevier.com/locate/cej

Novel bio-inspired metamaterials for athletes to achieve high energy absorption and sensing under sports-specific load

Zehao Tong [a,1], Cheng Lin [b,1], Liwu Liu [a,*], Yanju Liu [a,c,**], Jinsong Leng [b]

[a] Department of Astronautical Science and Mechanics, Harbin Institute of Technology (HIT), P.O. Box 301, No. 92 West Dazhi Street, Harbin, 150001, People's Republic of China
[b] Center for Composite Materials and Structures, Harbin Institute of Technology (HIT), P.O. Box 3011, No. 2 Yikuang Street, Harbin, 150080, People's Republic of China
[c] Suzhou Research Institute, Harbin Institute of Technology, Suzhou, 215100, People's Republic of China

ARTICLE INFO

Keywords:
Bio-inspired metamaterials
Athletes
Energy absorption
Deformation pattern
Sensing

ABSTRACT

In sports-specific movement, athletes are usually subjected to severe sports injuries in the eccentric phase of the stretch-shorten cycle, severely threatening their physical health, even ending their sports career, which may result in millions of dollars in additional expenses for national teams and sports clubs. Nevertheless, current sports equipment is not only unable to offer targeted cushioning for athletes but also incapable of monitoring exercise load to prevent sports injuries, owing to its simple structure and single functionality. Therefore, inspired by bionic features from bamboo, skeletal muscle, and cuttlefish bone, novel bio-inspired metamaterials with high energy absorption capabilities (401.21 J) were proposed in this study. In addition, by integrating a pure physical, cross-linked, double-network conductive hydrogel and bio-inspired metamaterials, a multifunctional insole with cushioning and sensing was developed in the study. It is of note that the bio-inspired multifunctional insole decreased the peak vertical ground reaction force to merely 76.6% of that of famous commercial running shoes, achieving an extra force reduction of up to 1.46 times body weight for targeted cushioning of athletes. Furthermore, it can also identify different locomotion from the stretch-shorten cycle to realize real-time exercise load monitoring. As a result, bio-inspired multifunctional insoles not only contributed to the scientific enhancement of sports-specific performance and personalized prevention of sports injury for athletes but also paved the way for upgrading and evolution of sports equipment.

1. Introduction

The activated muscle-tendon complex of athletes was rapidly and passively stretched in the eccentric phase of the stretch-shorten cycle (SSC) by the sports-specific load several times that of body weight while performing the difficult sports-specific technique. Due to the stress concentration of the musculoskeletal system, severe sports injuries frequently appear in this phase, such as Achilles tendon rupture and stress fracture, which can not only harm the physical health of athletes but also curtail their sports career. However, the national team and sports clubs need to spend millions of dollars on medical treatment, exercise rehabilitation, as well as conditioning for injured athletes. Thus, suitable sports equipment plays an essential role in preventing sports injury in SSC. Moreover, several drawbacks exist in current sports equipment, including its simple structure and single functionality, especially the lack of targeted cushioning for athletes during sports-specific movements. Additionally, exercise load monitoring can be achieved by incorporating sensors into sports equipment, providing precise information for enhancing sports performance and prevent sports injuries for athletes. Thus, it becomes crucial to design novel sports equipment with integrated cushioning and sensing capabilities providing high energy absorption and targeted cushioning for athletes.

Mechanical metamaterials offer possibilities for the structural designability of sports equipment, owing to their excellent mechanical properties, including negative stiffness, negative Poisson's ratio, bistability, negative thermal expansion, and lightweight ultrahigh strength, as well as energy absorption [1–15]. Mechanical metamaterials refer to a type of artificial material where the mechanical properties at the

* Corresponding author.
** Correspondence to: Y. Liu, Suzhou Research Institute, Harbin Institute of Technology, Suzhou, 215100, People's Republic of China.
E-mail addresses: liulw@hit.edu.cn (L. Liu), yj_liu@hit.edu.cn (Y. Liu).
[1] These authors contributed equally.

https://doi.org/10.1016/j.cej.2026.174178
Received 10 October 2025; Received in revised form 10 December 2025; Accepted 13 February 2026
Available online 11 March 2026

macroscale can be tailored via optimization and design of the geometry and structure of the unit cell at the mesoscale [1,3]. Besides, mechanical metamaterials offer extremely high freedom in structural design and superior energy-absorbing capacity, particularly bio-inspired metamaterials, as the motor organ of the specific bionic prototype (i.e., a mammal) shares similar mechanical properties with the musculoskeletal system of humans, which can probably enable outstanding targeted cushioning for athletes [2]. Previous studies have focused on designing novel bio-inspired metamaterials with high energy absorption by mimicking the structural features of dog pads, parrot beaks, bamboo, horseshoes, and starfish, etc. [2,16–19]. However, previous research only introduced the bionic feature to the specific component in the unit cell to optimize its geometry and design parameters. In order to maximize the energy absorption, it is essential to directly propose a novel unit cell via the hybridization of various bionics prototypes to arrange it to bio-inspired metamaterials, which was rarely reported in the existing studies.

In this study, by integrating the bionic prototype of bamboo, cuttlefish bone and skeletal muscle novel bio-inspired metamaterials with excellent energy absorbing capacity was proposed to enhance the designability of sports equipment (Fig. 1). The energy absorption, mechanical response, and the deformation pattern of bio-inspired metamaterials was investigated by carrying out quasi-static uniaxial compression test, cyclic compression test and finite element analysis. Bio-inspired metamaterials performed outstanding energy absorbing capacity (401.21 J). Additionally, a bio-inspired multifunctional insole (BMI) with integrated cushioning and sensing was developed through the incorporation of bio-inspired metamaterials and a pure physical, cross-linked, double network conductive hydrogel (PCMD) prepared using MXene, cellulose nanocrystals (CNC), and polyvinyl alcohol (PVA). It is worth noting that, when compared with famous commercial running shoes, BMI achieved an additional reduction in peak vertical ground reaction force, which was 1.46 times body weight. However, it can accurately distinguish between different locomotion, including fast SSC and slow SSC, therefore enabling real-time monitoring of exercise load.

2. Methodology

2.1. Design and fabrication of bio-inspired metamaterials

Nature provides various prototypes for energy-absorbing design. Bamboo can dissipate 409.30 J of energy from dynamic loading. The section of bamboo was featured as a double-ring structure with a thinned wall on the macro scale (Fig. 1a) [20–22]. Its culm was encompassed by a multi-layer epidermis. In the microstructure of bamboo, the number of vascular bundles was increased significantly from inside to outside, which was proportionally distributed in sparse layers, sub-intensive layers, and intensive layers (Fig. 1d) [23]. The gradient distribution of vascular bundles underpinned the high energy absorption capacity of bamboo. In accordance with the bamboo microstructure, a hierarchical concentric tubular structure and vascular bundles-like ribs with gradient distribution were designed and integrated to propose the unit cell of novel bamboo-inspired metamaterials (Bamboo) (Fig. 2c). Its walls were concentric and nested, comprising an outer tube, a secondary tube, and an inner tube. Between different layers of walls, vascular bundles-like ribs connected adjacent walls through the use of three beams. The number of ribs lowered significantly from the outside to the inside, while the ratio of the numbers of ribs in the outer tube and the secondary tube was specified to 10: 4. However, bamboo had 7 design parameters (i.e. d_1, d_2, d_3, t_1, t_2, t_r, θ), in which d_1 referred to the diameter of the outer tube, d_2 represented the diameter of the secondary tube, d_3 was the diameter of the inner tube, t_1 was the thickness of the outer tube, t_2 was the thickness of the secondary tube, t_r was the thickness of beams in ribs, and θ denoted angle between two beams in ribs, respectively (Table S1).

Similarly, excellent cushioning performance for skeletal muscle plays a crucial role in protecting brittle bones and vulnerable organs (Fig. 1c). The microstructure of skeletal muscle is typical of a hierarchical tubular structure [24]. Inside the muscle tissue, epimysium (outer layer) wrapped up a number of perimysium (secondary layer). Hundreds of muscle fibres acted as sub-inner layers, which were enclosed by perimysium. Many myofilaments (inner layer) were formed as muscle fibre cells (Fig. 1f) [24]. Under impact load, up to 90% of the energy was absorbed by the secondary and inner layers in the biological structure of

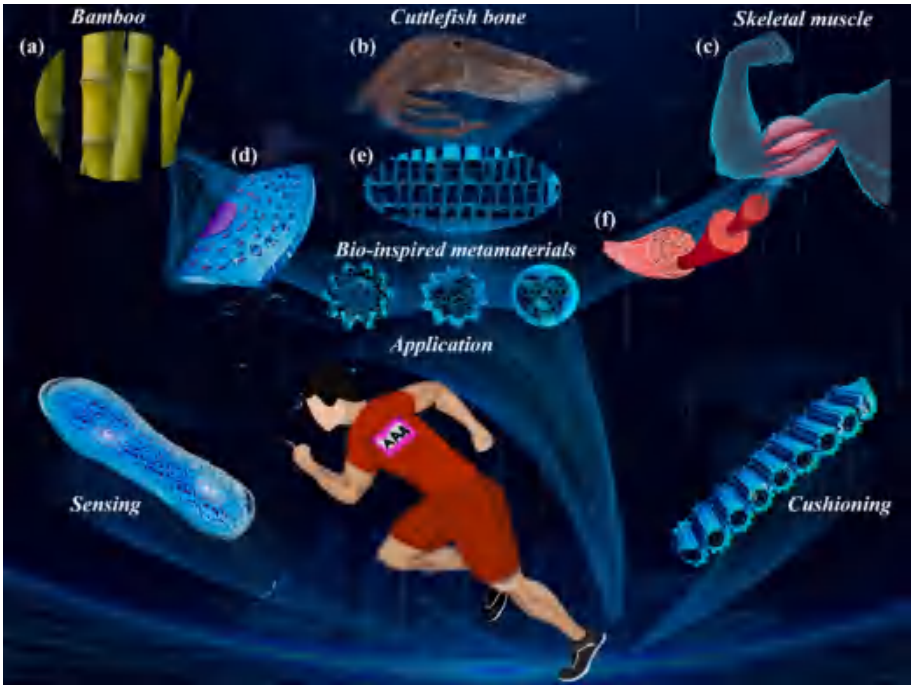

Fig. 1. Bio-inspired metamaterials focus on the cushioning and sensing in the competitive sports. Bionic prototypes of (a) Bamboo, (b) Cuttlefish bone, and (c) Skeletal muscle. Biological microstructure of (d) Bamboo, (e) Cuttlefish bone, and (f) Skeletal muscle.

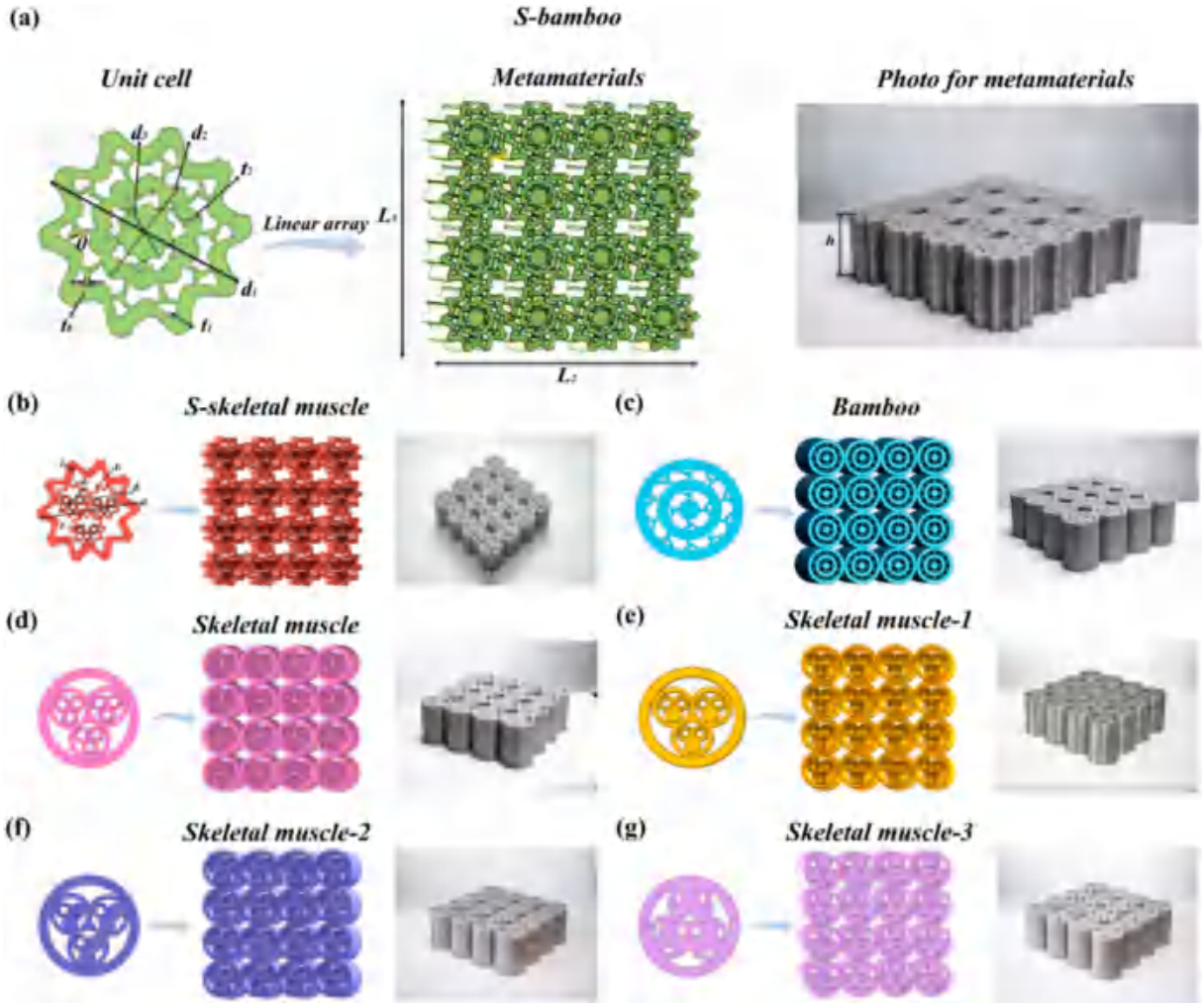

Fig. 2. The geometry configuration and design parameters of bio-inspired metamaterials. (a) S-bamboo. (b) S-skeletal muscle. (c) Bamboo. (d) Skeletal muscle. (e-g) Skeletal muscle-1, 2, 3. Bamboo: hierarchical concentric tubes mimicking bamboo; S-Bamboo: hierarchical concentric tubes inspiring bamboo with S-shaped wall imitating cuttlefish bone. Skeletal muscle: three tubes nested hierarchical structure inspiring skeletal muscle. S-skeletal muscle: three tubes nested hierarchical structure mimicking skeletal muscle with S-shaped wall imitating cuttlefish bone. Skeletal muscle-1: filled one inner tube in each secondary tube on the basis of skeletal muscle; Skeletal muscle-2: filled two inner tubes in each secondary tube based on skeletal muscle; Skeletal muscle-3: filled three inner tubes in each secondary tube based on skeletal muscle.

skeletal muscle [25]. Inspired by the hierarchical tubular structure of skeletal muscle, the unit cell of new skeletal muscle-inspired metamaterials (skeletal muscle) was designed (Fig. 2d), which was nested by the outer tube, the secondary tube, as well as the inner tube. The outer tube wrapped three secondary tubes, arranged in a circular array around the center of the unit cell. To explore the impact of the number of filled tubes on the energy-absorbing capacity of skeletal muscle, three unit cells (skeletal muscle-1, 2, 3) were designed by filling 1–3 inner tubes of skeletal muscle (Fig. 2e-g). Additionally, skeletal muscle, skeletal muscle-1, and skeletal muscle-2 had 6 design parameters, namely, the diameter of outer tube (d_1), the diameter of secondary tube (d_2), the diameter of inner tube (d_3), the thickness of outer tube (t_1), the thickness of secondary tube (t_2), the thickness of inner tube (t_3), respectively. Except t_3, all other parameters (i.e. d_1, d_2, d_3, t_1, t_2) were utilized as design parameters for skeletal muscle-3 (Table S1).

Depending on the excellent specific energy absorption of its skeleton, cuttlefish can resist huge pressure under the deep sea (Fig. 1b). At the micro-scale of cuttlefish bone, it can be found that lamellar septa were segmented by asymmetric "curved walls", forming a hierarchically porous structure (Fig. 1e) [26–30]. Based on the bionic feature of cuttlefish bone, a symmetric, S-shaped, curved wall was developed as an alternative to the tubular wall made from bamboo or skeletal muscle for enhanced energy absorption. Through the integration of the hierarchical concentric tubular structure, vascular bundles-like ribs and symmetric S-shaped curved wall, the unit cell of novel bamboo and cuttlefish bone-inspired metamaterials (S-bamboo) was designed (Fig. 2a). In the same way, a unit cell for new skeletal muscle and cuttlefish bone-inspired metamaterials (S-skeletal muscle) was designed by introducing the symmetric S-shaped curved wall to the hierarchical tubular structure (Fig. 2b). The design parameter of S-bamboo conformed to bamboo, while S-skeletal muscle shared the same parameters as skeletal muscle (Table S1). Considering the complexity and irregularity of the bionic prototype, simplification and abstraction were performed in the structural design of the unit cell [31]. In this study, seven types of bio-inspired metamaterials with 4 × 4 unit cells were formed via the linear array along the X direction and Y direction, which show a uniform height (h = 48 mm), length (L_1 = 160 mm) and width (L_2 = 160 mm) (Fig. 2).

The bio-inspired metamaterials were fabricated using a fused deposition modelling (FDM) 3D printer (Bambu Lab A1, China) (Fig.S8). Thermoplastic polyurethane (TPU) 95A filament (Bambu Lab™, China) was selected as the printing material of bio-inspired metamaterials. A 0.4 mm nozzle and a 0.6 mm nozzle were employed in the printing process (Table S2). The nozzle temperature was specified at 230–253 °C,

and the temperature of the printing platform was set as 45–65 °C during the fabrication process. The printing speed and layer thickness were 35–50 mm/s and 0.25–0.4 mm, respectively.

2.2. Mechanical test of bio-inspired metamaterials

Quasi-static uniaxial radial and axial compression tests were carried out at room temperature using a universal testing machine (WDW-300, Sanjiang Testing Technology Co., Jinan, China) with a 300 kN load cell. Bio-inspired metamaterials were placed at the center of the compression plate. It was pre-loaded up to 2 N with a pre-loading speed of 20 mm/min when the compression plate contacts its upper surface. Displacement control setup (radial compression displacement: 140 mm, axial compression displacement: 45 mm) was employed with a normal loading speed of 30 mm/min. The cyclic compression test was conducted in the radial direction via a universal testing machine (WDW-300, Sanjiang Testing Technology Co., Jinan, China) with a 300 kN load cell [32,33]. Ten successive cycles were performed at a speed of 30 mm/min for loading and unloading with a compression displacement of 9.6 mm.

Here, the mechanical parameters for energy absorption were calculated [34]. Energy absorption (EA) was worked out, in light of the area under the force-displacement curve:

$$\mathrm{EA} = \int_0^d F(\mathrm{x})d\mathrm{x} \tag{1}$$

where d represents the effective compressive displacement of the specimen and F is the uniaxial compression force.

Specific energy absorption (SEA), a parameter quantifying the amount of energy absorbing efficiency of bio-inspired metamaterials, was calculated as the ratio of EA and specimen mass (m):

$$\mathrm{SEA} = \frac{\mathrm{EA}}{m} \tag{2}$$

Crash load efficiency (CLE) was defined as the ratio of mean crash force (MCF) and peak crash force (PCF):

$$\mathrm{CLE} = \frac{\mathrm{MCF}}{\mathrm{PCF}} \times 100\% \tag{3}$$

where PCF denotes the peak force of specimens under uniaxial compression, and MCF represents the ratio of EA and effective compressive displacement (d). In general, PCF refers to the initial peak force, indicating the first peak in the force-displacement curve during the compressive process [35].

2.3. Numerical simulation of bio-inspired metamaterials

The quasi-static compression process was simulated using Abaqus/Explicit (Dassault, MA, USA) to analyze the distribution of von Mises stress. The material parameters for TPU 95 A were specified according to the stress-strain curve of each bio-inspired metamaterials obtained from the uniaxial quasi-static compression (Table S6). The finite element model consisted of two rigid plates, modeled as 3D discrete rigid bodies, and bio-inspired metamaterials in between, modeled as a 3D deformable body (Fig. 5a, Fig. 6a). The bottom rigid plate was fully constrained through its center of mass (COM) (Fig.S23, Fig.S24). The upper rigid plate was subjected only to vertical displacement at its COM. Other degrees of freedom for the upper rigid plate were constrained. “Hard” contact was set up in normal behavior, while a penalty of 0.2 was specified in tangential behavior. The mesh of the finite element model was created and optimized using Hypermesh version 2017 (Altair, MI, USA). The bio-inspired metamaterials were meshed using linear hexahedron elements (C3D8), linear tetrahedron elements (C3D4), whereas linear hexahedron elements (C3D8) were used for two rigid plates.

3. Results and discussion

3.1. Compressive property of bio-inspired metamaterials

Compressive force-displacement curves under radial load exhibited an initial rise, followed by a rapid increase until reaching the peak force (Fig. 3a-c). In the compressive process, the stiffness of S-bamboo was greater than that of bamboo, while S-skeletal muscle performed a smaller stiffness than skeletal muscle. In addition, it can be found that the stiffness of skeletal muscle was larger than that of skeletal muscle-1, 2, and 3. In axial compression, force-displacement curves exhibited a different pattern, which comprised a linear elastic region represented as a rapid rise prior to the yield point, a plateau region represented as a drop after the yield point, followed by a gradual rise, and a densification region indicated as a rapid increase until reaching the peak force (Fig. 3d-f). During the compressive process, S-bamboo exhibited larger stiffness than that of bamboo, whereas the stiffness of S-skeletal muscle was smaller than that of skeletal muscle. Besides, skeletal muscle also exhibited a greater stiffness than skeletal muscle-1, 2, and 3.

During radial compression, the stress-strain curves implied that S-bamboo exhibited a greater yield stress than that of bamboo, but the yield stress of S-skeletal muscle was shown to be smaller than that of skeletal muscle (Fig. 3g-i). Furthermore, skeletal muscle exhibited higher yield stress than skeletal muscle-1, 2, and 3. In axial compression, it can be found that the yield stress of S-skeletal muscle was greater than that of skeletal muscle, while S-bamboo also revealed a higher yield stress than that of bamboo (Fig. 3j-l). Additionally, the yield stress of skeletal muscle-1 was larger than that of skeletal muscle and skeletal muscle-2 and 3.

To comprehend the deformation pattern of bio-inspired metamaterials, the specimens were observed under radial load at compressive strains of 21.875%, 43.75%, 65.62%, and 87.5% (Movie S1). For bamboo, the ribs in the vertical direction and the adjacent wall were firstly deformed, followed by a significant compressive deformation of the remaining ribs until reaching the densification (Fig. S9). Interestingly, the ribs supported the tubular walls and transferred the vertical load in radial compression [36,37]. By contrast, S-bamboo performed another deformation pattern, which exhibited a slightly lateral global buckling before compressing to the densification (Fig. S10), probably because the ribs of S-bamboo provide the multidirectional channel for load transmission as well as effective support for adjacent S-shaped walls contributing to the compressive resistance and the stability of the energy absorbing process [28–30,38,39]. However, skeletal muscle experienced a different pattern in the compressive process. First, the outer tube was significantly deformed, probably due to its large stiffness (Fig. S11) [24,25]. It is followed by the deformation of the lowest secondary and inner tubes, perhaps because the smaller contact area between the lowest tube and the adjacent wall weakens the load transmission. On the contrary, S-skeletal muscle exhibited lateral global buckling until it was compressed to densification, perhaps because the load was concentrated on the middle part of the surface of S-shaped walls and poor load transmission triggered the global buckling (Fig. S12) [30]. Moreover, skeletal muscle-1, 2, 3 shared similar deformation patterns, exhibiting significant deformation of the lowest secondary and inner tubes before densification (Fig. S13–15). It was suggested that the number of filled tubes for skeletal muscle might not relate to the compressive resistance of the radial load.

The deformation mode of bio-inspired metamaterials under axial load was observed at the compressive strains of 23.44%, 46.875%, 70.31%, and 93.75%. During the compressive process of bamboo, the middle part of the tubular walls was firstly deformed, and then the specimen exhibited global buckling (Fig. S16) [40,41]. The global buckling of bamboo can be caused by a discrepancy in the number of ribs between the outer tube and the secondary tube, which may result in the non-uniform deformation to weaken the stability of the deformation process [36]. Comparatively, S-bamboo exhibited a distinct deformation

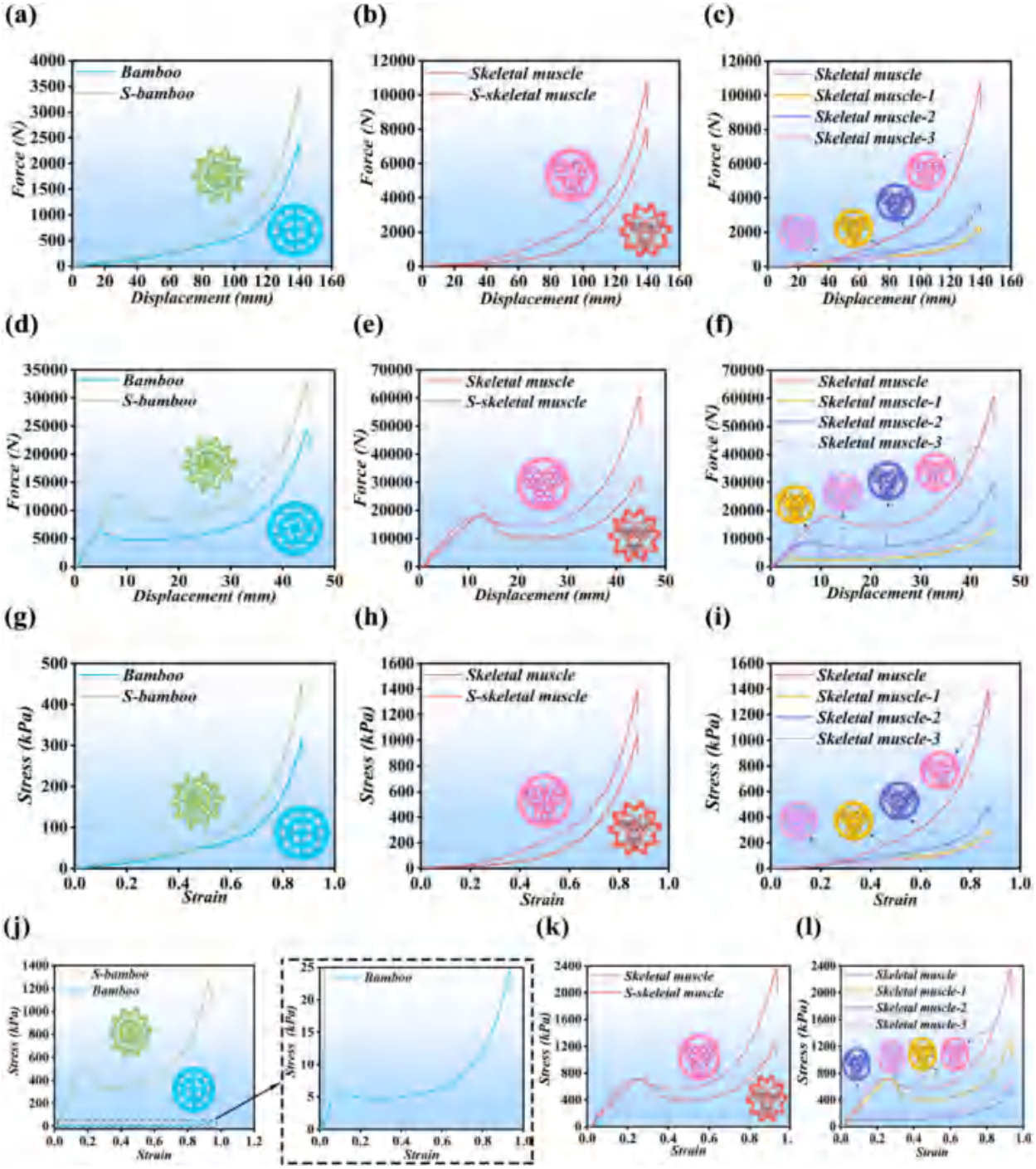

Fig. 3. Mechanical response of bio-inspired metamaterials under quasi-static compression. Force-displacement curve of (a) Bamboo versus S-bamboo, (b) Skeletal muscle versus S-skeletal muscle, (c) Skeletal muscle versus skeletal muscle-1, 2, 3 in radial compression. Force-displacement curve of (d) Bamboo versus S-bamboo, (e) Skeletal muscle versus S-skeletal muscle, (f) Skeletal muscle versus skeletal muscle-1, 2, 3 in axial compression. Stress-strain curve of (g) Bamboo versus S-bamboo, (h) Skeletal muscle versus S-skeletal muscle, (i) Skeletal muscle versus skeletal muscle-1, 2, 3 in radial compression. Stress-strain curve of (j) Bamboo versus S-bamboo, (k) Skeletal muscle versus S-skeletal muscle, (l) Skeletal muscle versus skeletal muscle-1, 2, 3 in axial compression.

pattern under axial load, characterized by uniform deformation of the S-shaped wall followed by lateral global buckling (Fig. S17). In the compressive process, the uniform deformation of the S-shaped wall may contribute to the compressive strength and delay global buckling, therefore supporting the energy-absorbing capacity of S-bamboo [42]. Similarly, skeletal muscle also experienced an even deformation of the tubular wall followed by a subsequent global buckling, accounting for its high energy absorption under axial load (Fig. S18).When compared with skeletal muscle, a different deformation pattern occurred in S-skeletal muscle, which exhibited the global buckling in the posteroanterior direction during the axial compression, probably owing to the asymmetric distribution of secondary and inner tubes and the absence of interlaminar ribs, which was adverse to the load transmission and energy-absorbing capacity (Fig. S19) [40]. However, Skeletal muscle-1, 2, 3 exhibited a similar deformation pattern, characterized by a significant deformation of the middle part of the tubular wall, followed by global buckling, which may be resulted from the inconsistency in buckling resistance between filled and unfilled tubes (Fig. S20–22).

During the radial compression, the EA of S-bamboo (95.46 J) is significantly better than that of bamboo (67.76 J), while skeletal muscle (302.16 J) is 1.53 times that of S-skeletal muscle (197.18 J) (Fig. 4a, Table S3). It was suggested that the S-shaped wall contributes significantly to the energy-absorbing capacity in S-bamboo, rather than in S-skeletal muscle under radial load. Moreover, the EA value of skeletal muscle was 3.63 times that of skeletal muscle-1 (83.31 J), 2.4 times that of skeletal muscle-2 (125.73 J), and 4.1 times that of skeletal muscle-3 (73.76 J). Obviously, the number of filled inner tubes was shown to be irrelevant to energy-absorbing capacity in the radial compression. In axial compression, the EA value of skeletal muscle (401.20 J) was 3.26 times that of S-skeletal muscle (325.54 J). On the contrary, S-bamboo (263.52 J) was 1.75 times that of bamboo (150.74 J) on EA (Fig. 4e, Table S4). It was indicated that the S-shaped wall performed more effective EA behavior in S-bamboo than that in S-skeletal muscle under axial load. Additionally, the EA of skeletal muscle was 1.03 times that of skeletal muscle-1 (388.61 J), while skeletal muscle-1 was remarkably greater than skeletal muscle-2 (101.99 J), and skeletal muscle-3 (162.71 J). It was suggested that the filled inner tubes may weaken the energy-absorbing property under axial load.

The SEA of skeletal muscle (915.65 J/kg) was the highest under radial compression, which was 3.89 times that of skeletal muscle-1 (235.34 J/kg), 2.23 times that of skeletal muscle-2 (410.89 J/kg), and 3.2 times that of skeletal muscle-3 (285.89 J/kg) (Fig. 4b, Table S3). The possible reason is that filled inner tubes decrease the porosity of the unit cell, resulting in a greater mass of skeletal muscle-1, 2, 3. Besides, S-bamboo exhibited better SEA under radial load, and its SEA (253.89 J/kg) was 1.42 times that of bamboo (178.32 J/kg). The possible reason is that S-shaped walls increase the porosity of the unit cell, resulting in a smaller mass of S-bamboo. On the other hand, the difference in SEA between S-bamboo and bamboo may be attributed to the variation of rib thickness [36]. Additionally, skeletal muscle exhibited a larger SEA in radial compression, and its SEA (915.65 J/kg) was 1.68 times that of S-skeletal muscle (546.22 J/kg), perhaps because the S-shaped wall led to the different porosity of the unit cell.

Similarly, skeletal muscle also performed the highest SEA under axial load, and its SEA (1215.78 J/kg) was 1.11 times that of skeletal muscle-1 (1097.77 J/kg), 3.65 times that of skeletal muscle-2 (333.29 J/kg), and 1.93 times that of skeletal muscle-3 (630.65 J/kg) (Fig. 4f, Table S4). The possible reason is that the absence of filled inner tubes resulted in a smaller mass of skeletal muscle. However, S-bamboo exhibited greater SEA than bamboo in axial compression, and its SEA (700.84 J/kg) was 1.77 times that of the corresponding value of bamboo (396.69 J/kg). The possible reason is that S-shaped walls increase the porosity of the unit cell, resulting in a smaller mass of S-bamboo. In addition, skeletal muscle (1215.78 J/kg) was 1.35 times that of S-skeletal muscle (901.78 J/kg) under axial load, perhaps due to the different mass between skeletal muscle and S-skeletal muscle.

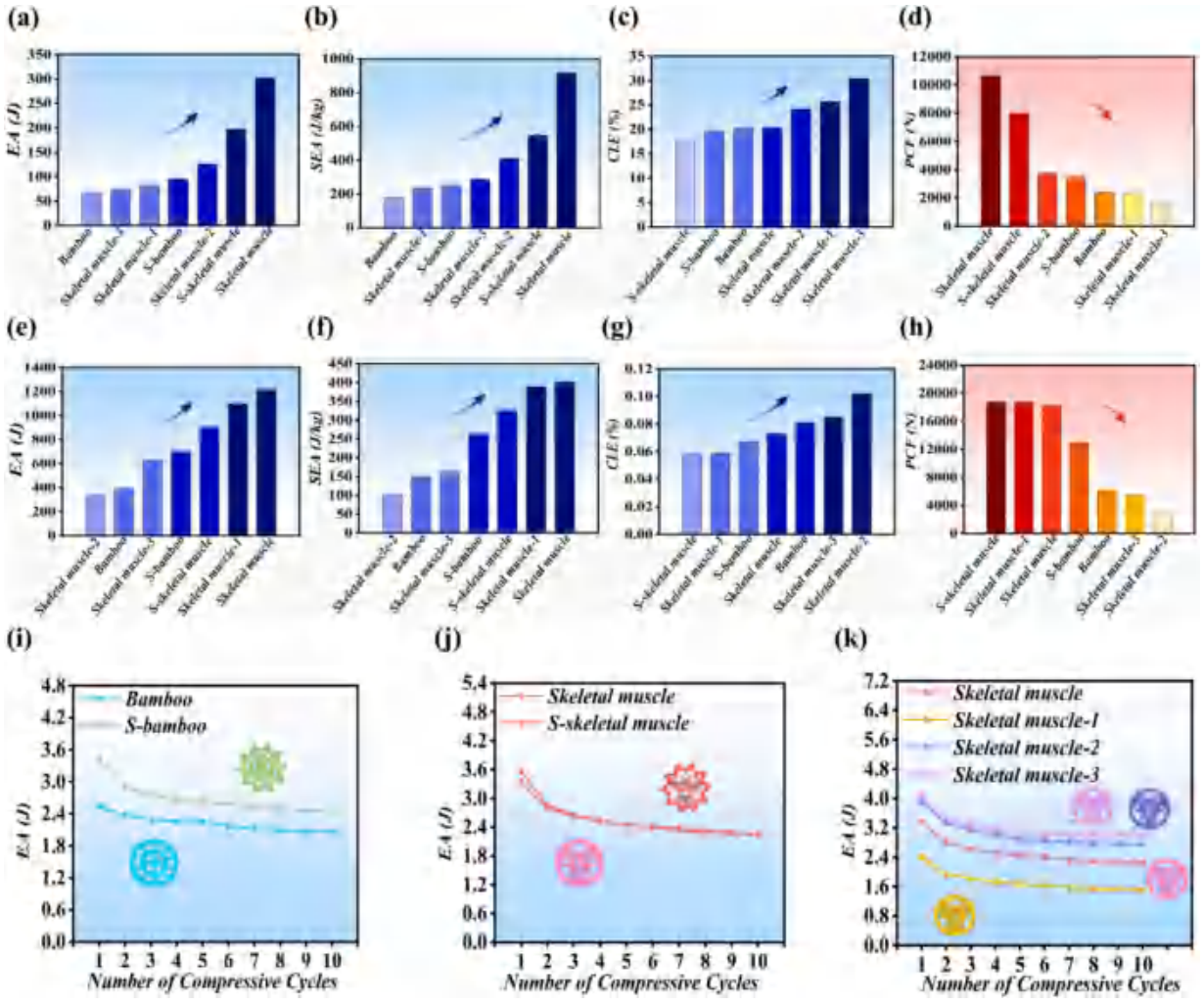

Fig. 4. Energy absorption of bio-inspired metamaterials. (a) EA, (b) SEA, (c) CLE and (d) PCF in radial compression. (e) EA, (f) SEA, (g) CLE and (h) PCF in axial compression. Energy absorption for (i) Bamboo versus S-bamboo, (j) Skeletal muscle versus S-skeletal muscle, (k) Skeletal muscle versus skeletal muscle-1, 2, 3 in cyclic compression. EA: Energy absorption; SEA: Specific energy absorption; CLE: Crash load efficiency; PCF: Peak crash force; MCF: Mean crush force.

The results suggested that both skeletal muscle (1215.78 J/kg) and skeletal muscle-1 (1097.77 J/kg) exhibit higher SEA than the cuttlebone-like structure (424 J/kg), the Gyroid structure (916 J/kg), and the Schwartz Primitive structure (687 J/kg) reported by Cui et al. [53] under axial compression. Notably, the SEA of skeletal muscle was 2.87-fold that of the cuttlebone-like structure, 1.33-fold that of the Gyroid structure, and 1.77-fold that of the Schwartz Primitive structure, indicating superior energy-absorbing property. Besides, skeletal muscle-1 also exhibited good energy absorption performance, and its SEA was 2.59 times that of the cuttlebone-like structure, 1.2 times that of the Gyroid structure, and 1.6 times that of the Schwartz Primitive structure.

In the radial compression, S-skeletal muscle (17.66%) exhibits a slightly smaller CLE than skeletal muscle (20.29%) (Fig. 4c, Table S3). It was indicated that the S-shaped wall may decrease the CLE of skeletal muscle. One possible reason is that although the PCF of S-skeletal muscle (8000 N) was merely 0.75 times that of skeletal muscle (10,670 N), the S-skeletal muscle (1413 N) has lower MCF than skeletal muscle (2165.28 N), contributing to the sharp drop after reaching its initial peak and damage its capacity to continue to absorb energy (Fig. 4d, Table S3). Similarly, the CLE of S-bamboo (19.68%) was also 2.48% smaller than bamboo (20.18%), even though it (683.99 N) was shown to be greater than that of bamboo (485.27 N) on MCF. The possible reason is that owing to the different PCF values, S-bamboo (3475 N) experienced a sharper decrease than bamboo (2405 N) after reaching the PCF, which can result in poor stability [35,36]. Although skeletal muscle-3 (528.59 N) had the lowest MCF, the CLE of skeletal muscle-3 (30.38%) was 1.26 times that of skeletal muscle-2 (24.11%) and 1.18 times that of skeletal muscle-1 (25.68%), while skeletal muscle-1 and 2 were also remarkably higher than skeletal muscle (20.29%) on CLE. On the contrary, skeletal muscle-3 owned the lowest PCF (1740 N), while both skeletal muscle-1 (2325 N) and skeletal muscle-2 (3735 N) showed remarkably lower PCF than skeletal muscle (10,670 N). The possible reason is that the number of filled inner tubes showed a positive relationship to CLE, which was negatively associated with PCF. In this way, high CLE and low PCF indicated a more stable energy-absorbing process and lower PCF.

During axial compression, the CLE of S-skeletal muscle (0.058%) was merely 0.79 times that of skeletal muscle (0.073%), while S-bamboo also has a smaller CLE (0.067%) than bamboo (0.081%) (Fig. 4g, Table S4). The possible reason is that even though S-bamboo (8.78 N) has higher MCF than bamboo (5.02 N), the PCF of S-bamboo (12,945 N) and S-skeletal muscle (18,690 N) was higher than bamboo (6185 N) and skeletal muscle (18,245 N) to varying degrees, due to the existence of S-shaped wall (Fig. 4h, Table S4). In this way, a significant drop after the first peak was caused by excessive PCF, weakening the stability and the continuity of energy absorption. Skeletal muscle-2 (0.102%) was 1.2 times that of skeletal muscle-3, 1.40 times that of skeletal muscle (0.073%) and 1.73 times that of skeletal muscle-1 (0.059%) on CLE, while it exhibits significantly lower PCF (2835 N) than skeletal muscle-3 (5430 N) and skeletal muscle-1 (18,690 N) (Fig. 4g-h) (Table 4). Obviously, even if its MCF (2.91 N) was significantly lower than skeletal muscle (13.37 N), skeletal muscle-1 (11.10 N), and skeletal muscle-3 (4.65 N), skeletal muscle-2 still performed a more stable energy absorbing process, since two filled inner tubes may contribute to the uniform distribution of axial load.

3.2. Cyclic compressive property of bio-inspired metamaterials

In cyclic compression, the EA of all bio-inspired metamaterials exhibited a significantly drop in the 2nd cycle, followed by a gradual decrease from the 2nd cycle to the 3rd cycle, and finally remained almost steady from the 4th cycle onwards until the 10th cycle (Fig. 4i-k, Table S5). The EA of S-skeletal muscle decreased most significantly (1.33 J) from the 1st to 10th cycle, whereas EA in the last cycle was merely 0.63 times that of the EA in the first cycle. Comparatively, the reduction of EA for skeletal muscle-1, 2, 3, and skeletal muscle was 1.11 J, 1.16 J, 0.89 J, and 1.11 J, respectively. The EA of bamboo decreased most gradually (0.47 J), and its EA at the last cycle was 0.82 times that of its EA at the 1st cycle. S-bamboo (0.96 J) revealed a more significant trend than bamboo during the decline in EA, while its EA in the last cycle was only 0.72 times that of its value in the first cycle. Moreover, it appeared to be that the S-shaped wall may weaken the repeatability of energy-absorbing capacity.

3.3. Finite element simulation of bio-inspired metamaterials

The finite element model was validated with the deformation behavior of specimens that were found in the quasi-static compression test. The deformation pattern of numerical simulation shows good agreement with observation in the experiment (Fig. 5). FEA result suggested the distribution feature of Von Mise stress for bio-inspired metamaterials under radial compression. For bamboo, stress firstly accumulated at specific zones in the upper two layers, particularly in the ribs in the vertical direction within the outer tube, all ribs in the secondary tube, and the intersections between them and the tubular wall, while the stress also concentrated on the ribs at the top of the adjacent layer (Fig. 5b). Next, stress was mainly concentrated on all ribs in the vertical direction in each layer, even though the high stress zone also existed in partial ribs in the horizontal direction. Consequently, the transmission of transverse load was significantly slower than vertical load, which harmed the EA capacity of bamboo, owing to the asynchronous deformation of the ribs. On the contrary, S-bamboo exhibited different characteristics of stress distribution. Obviously, the high stress zone was predominantly localized to most of the ribs in the upper three layers first (Fig. 5c). Subsequently, the stress concentration zone was expanded in multiple directions and spread from the ribs to adjacent walls in all layers. As a result, the S-shaped wall and the ribs poly-directionally and synchronously transmitted load under radial compression, supporting the high EA capacity of S-bamboo. At first, the high stress zone was mainly localized on the outer, secondary and inner tubes in the upper three layers of skeletal muscle (Fig. 5d). Then, the stress concentration zone was transferred to the secondary tubes and inner tubes in all layers, while stress was uniformly distributed on the outer tube. Similarly, S-skeletal muscle shared an analogous pattern of stress distribution with skeletal muscle. In the same way, the stress was firstly concentrated on the specific zone in the upper two layers, the tubular wall of each level (Fig. 5e). Subsequently, the stress concentration zone merely accumulated in the secondary and inner tubes of all layers. However, the high stress zone of skeletal muscle was more uniformly distributed than S-skeletal muscle, explaining its higher EA capacity in radial compression. In terms of skeletal muscle-1, stress firstly accumulated at unfilled inner tubes in the upper three layers, as well as the intersection of the outer tube and secondary tubes (Fig. 5f). This is followed by stress concentration on unfilled inner tubes in all layers. Regarding skeletal muscle-2, the high stress zone was first located at the unfilled inner tubes and the outer tube in the upper three layers. Then, it was spread to the unfilled inner tubes and the outer tube of all layers (Fig. 5g). In terms of skeletal muscle-3, stress was mainly concentrated at the inter-tube intersection during the radial compression (Fig. 5h). However, it has been found that the high stress zone frequently appears on unfilled inner tubes, which may clarify the inconsistent EA capacity among skeletal muscle-1, 2, 3.

The result of numerical simulation suggested the distribution characteristic of Von Mises stress for bio-inspired metamaterials under axial compression (Fig. 6). At first, the high stress zone was localized at the bottom of the bamboo (Fig. 6b). This is followed by the stress concentration at the top and the bottom edges. Therefore, the uneven stress distribution of bamboo may weaken its EA capacity. For S-bamboo, stress first accumulated at the top and the bottom edges, and the bump of the central zone (Fig. 6c). Subsequently, except for a few zones of stress concentration at both ends, stress was almost uniformly distributed on S-bamboo, thus supporting its superior EA capacity. The potential reason is that the high stress zone on the bump contributed to the

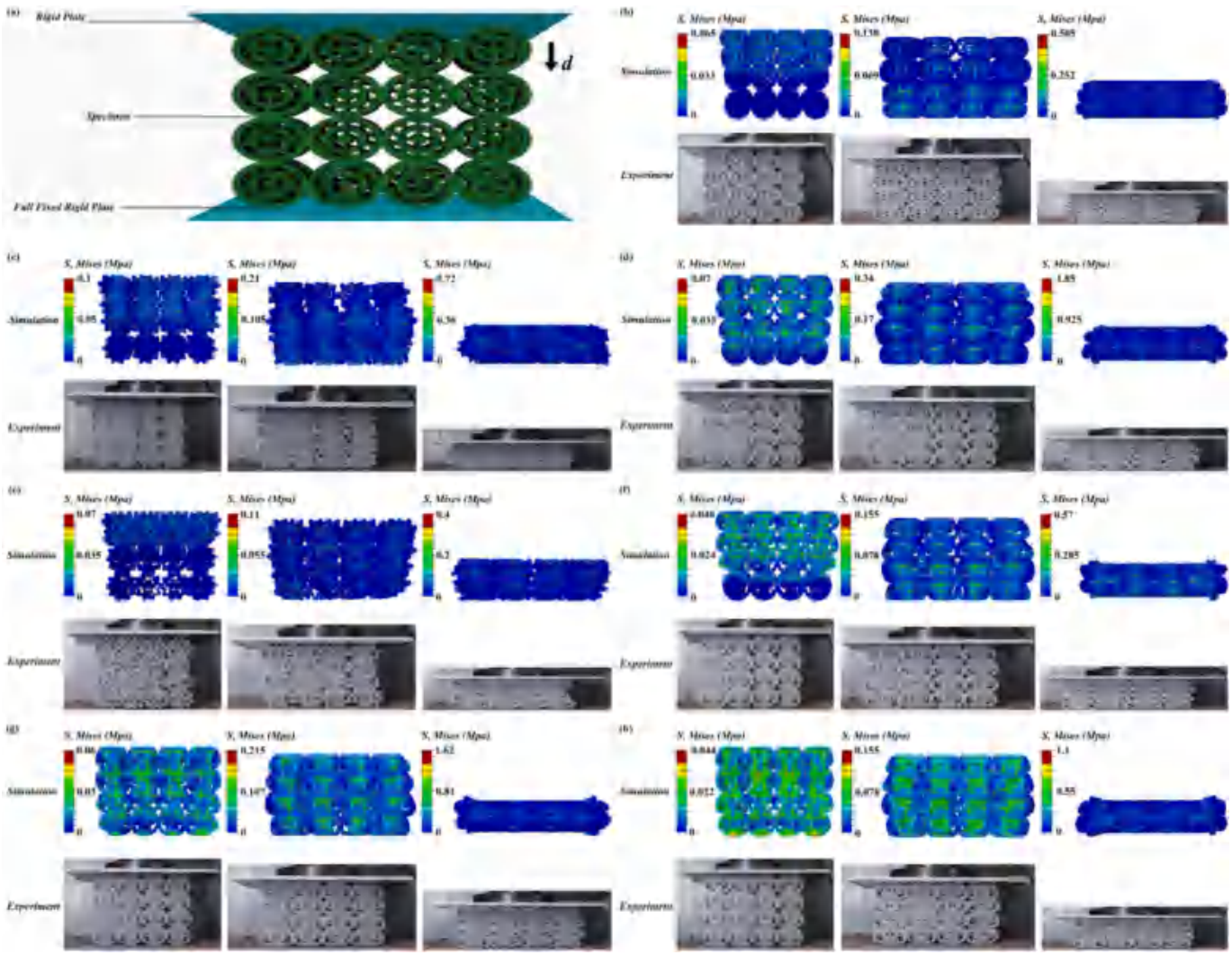

Fig. 5. Comparison on deformation process between finite element analysis and experiment in radial compression. (a) Finite element model for bio-inspired metamaterials under radial compression. (b) Bamboo. (c) S-bamboo. (d) Skeletal muscle. (e) S-skeletal muscle. (f) Skeletal muscle-1. (g) Skeletal muscle-2. (h) Skeletal muscle-3.

beforehand deformation of S-shaped walls to delay the global buckling of S-bamboo. For skeletal muscle, stress was predominantly accumulated at the top and the bottom edges, as well as scattered zone on the surface of tubular walls first (Fig. 6d). This was followed by the stress concentration along the folded zone. By contrast, S-skeletal muscle performed another pattern under axial load, which achieved almost uniform stress distribution after undergoing a phase in which the stress concentrated on the bump, the top, and the bottom edges of the S-shaped wall (Fig. 6e). Consequently, inconsistent patterns of stress concentration may result in different EA capacity between skeletal muscle and S-skeletal muscle. Skeletal muscle-1, 2, 3 shared the analogous pattern of stress distribution under axial compression (Fig. 6f-h).Clearly, high stress zones first localized at the top and the bottom edges. Subsequently, stress accumulated at the folded zone to varying degrees, probably owing to different EA capacity among skeletal muscle-1, 2, 3.

4. Applications

When the athlete performed sports-specific techniques, the musculoskeletal system was subjected to excessive impact force in the eccentric phase of SSC, which was up to 5.3 times that of body weight (BW) [43,44]. To minimize the impact force, four types of BMI with uniform sizes (length: 351 mm, width: 106 mm, thickness: 40 mm), namely bamboo bionic metamaterials insole (BBM-I), S-shaped bamboo bionic metamaterials insole (SBBM-I), skeletal muscle bionic metamaterials insole (SMBM-I) and S-shaped skeletal muscle bionic metamaterials insole (SSMBM-I), were fabricated (Fig. 7a-d); printing process of BMI was shown in supporting information. However, the famous commercial running shoes (RS) (Nike Free RN, USA) were selected as the control (Fig. S25).

The drop jump (DJ) test was carried out to examine the cushioning performance of BMI, because DJ is a typical SSC, which was strongly related to sports performance or injury risk in athletes from most events, such as basketball, track and field, rugby, soccer, volleyball, etc. [45–50]. To exclude the influence of diversity of training experience, one healthy student of physical education, who has no injury history on the lower extremity or joints, was recruited as a subject to the DJ test (gender: male, height: 183 cm, body mass: 88.4 kg), and did not intake alcohol or caffeine within 48 h. 30 cm and 60 cm were adopted as drop height (Table S7). 28 reflective markers were placed over the anatomical landmarks of lower limbs for static calibration, while 24 markers were preserved for motion analysis (Fig. 7e, Table S8).

To start the drop action, the subject was asked to raise the dominant leg, naturally lean forward, and drop freely. The subject needs to jump vertically as explosively as possible, while both feet touch the force platform (Fig. 7f, Fig. S26–28) [51]. The subject must keep akimbo

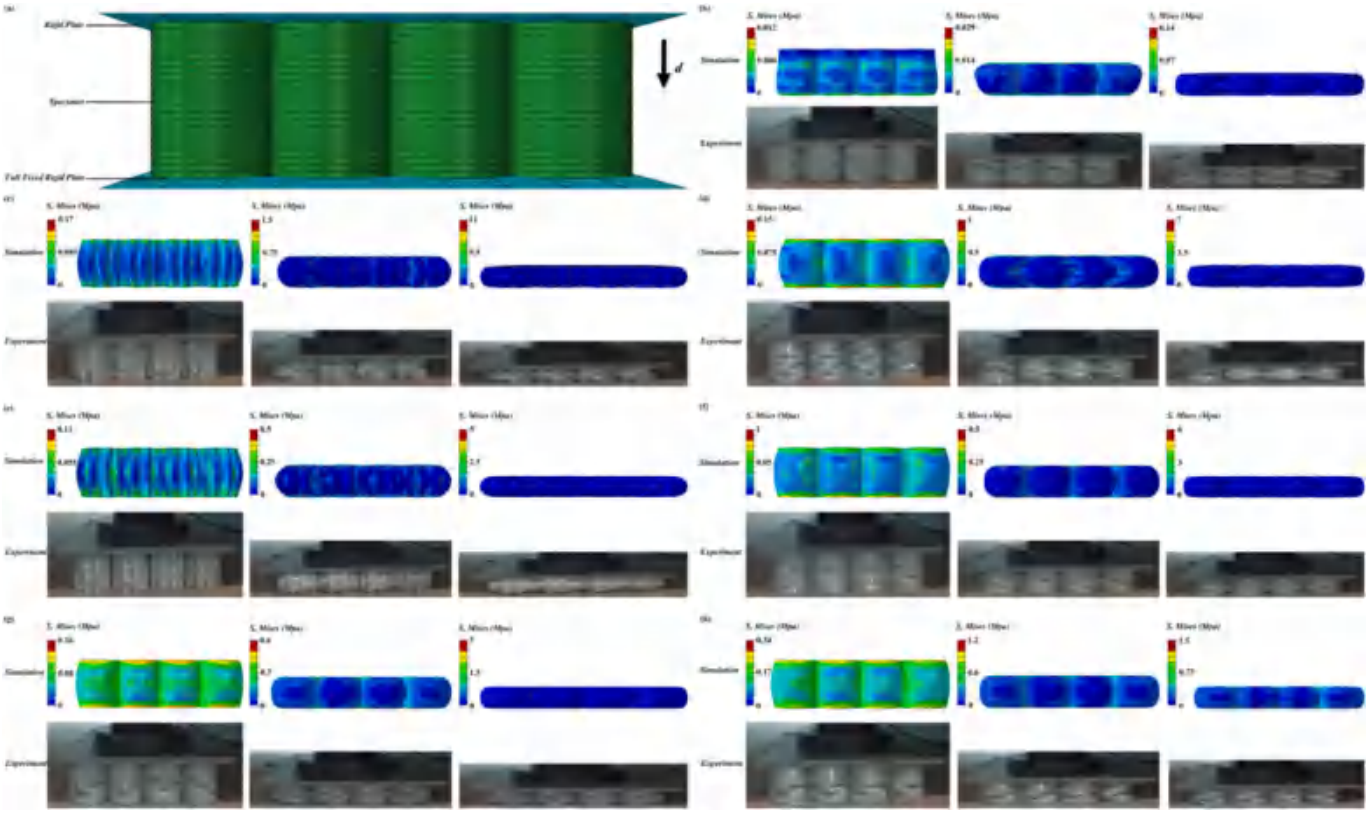

Fig. 6. Comparison on deformation process between finite element analysis and experiment in axial compression. (a) Finite element model for bio-inspired metamaterials under axial compression. (b) Bamboo. (c) S-bamboo. (d) Skeletal muscle. (e) S-skeletal muscle. (f) Skeletal muscle-1. (g) Skeletal muscle-2. (h) Skeletal muscle-3.

during the whole process of DJ. Kinematics data and vertical ground reaction force (vGRF) data were collected by a motion capture system (Vicon Bonita, UK) with a sampling frequency of 100 Hz, and a force platform (ATMI, USA) at 1000 Hz, respectively. Peak of vGRF data before the maximum flexion of the knee joint was commonly used to quantify the cushioning capacity of insoles because it indicates the maximal impact force in the eccentric phase (Fig. S29–38) [52]. Two DJs were performed on each drop height to choose the data with the highest flight height. Subsequently, the vGRF profile was normalized by the subject's body weight (BW) to minimize the effect of individual differences. To exclude the contribution of footwear on cushioning performance, the BMI was only fixed to the subject's foot by adhesive tape, not placed in footwear.

Fig. 7h-i shows the force-time profile at a drop height of 30 cm and 60 cm. Along with drop height increases, vGRF was increased significantly (Table S9). It indicated that a higher drop height aggravated the risk of sports injury. Peak vGRF data from different types of insoles in DJ were summarized in Fig. 7g. Interestingly, all insoles have a lower peak vGRF than RS (4.69 BW) at a drop height of 30 cm, which was only 0.76–0.89 times that of RS. It indicates that the BMI has excellent cushioning performance at the lower drop height. At a drop height of 30 cm, the peak vGRF of SSMBM-I (3.61 BW) is the lowest, which was significantly lower than that of SMBM-I (4.16 BW). Similarly, the peak vGRF of SBBM-I (3.8 BW) was also lower than that of BBM-I (4.18 BW) at a drop height of 30 cm. It demonstrated that the design of the S-shaped wall can improve the cushioning capacity at the lower drop height. However, all insoles still showed better cushioning capacity than RS (6.24 BW) at a height of 60 cm, whose peak vGRF was only 0.77–0.96 times that of running shoes. At higher drop heights, the peak vGRF of SBBM-I (4.78 BW) was significantly lower than that of BBM-I (5.99 BW). By contrast, SSMBM-I (4.86 BW) was higher than SMBM-I (4.78 BW) on peak vGRF. It concluded that the S-shaped wall can enhance the cushioning capacity in SBBM-I, instead of SSMBM-I, at higher drop height.

The results demonstrated that the peak vGRF of SBBM-I and SMBM-I at the drop height of 60 cm (4.78 BW) in this study was smaller than that of the running shoes in the drop jump test from 50 cm (4.96 BW) reported by Wang et al. [54], that of the cat pad-inspired shoes in the drop landing test from 40 cm (4.88 BW) reported by Wang et al. [55], and that of military boots in the drop landing test from 54 cm (6.2 BW) reported by Aziz et al. [56]. Although a higher drop height was selected in this study, SBBM-I and SMBM-I still exhibited better cushioning performance, with their peak vGRF being only 77.1% of the corresponding value of military boots, 96.37% that for running shoes, and 97.9% that for cat pad-inspired shoes (Fig. 7j, Table S10).

To investigate the cyclic cushioning performance of BMI, six healthy collegiate athletes, including one sprinter, three football players, one rugby player, and one bodybuilder, were recruited as subjects for the cyclic DJ test (gender: 3 male and 3 female, height: 172.7 $\pm$ 5.43 cm, body mass: 71.68 $\pm$ 8.12 kg). Before the test, a 5-min jogging was arranged for warm-up, and then a pair of BMI was fixed to the subject's feet using adhesive tape. After a 1-min rest, 30-cm DJs were first performed in a single set of 5 repetitions (1 $\times$ 5) with a 60-s intra-set rest (Fig. S44). After a 5-min rest, 60-cm DJs were carried out in one set of 5 repetitions (1 $\times$ 5) with a 60-s intra-set rest. After another 5-min rest, the cyclic DJ test of the other BMI was conducted. The average of peak vGRF in the eccentric phase across all subjects was calculated to assess the cyclic cushioning property of BMI. However, the peak vGRF data in the eccentric phase of the commercial sports shoes (CSS) (Do-win MR3515, China) were selected as the control.

The results demonstrated that all BMIs maintained a stable cushioning performance throughout cyclic drop jumps from 30 cm (Fig. 7k, Table S11). Relative to the first cycle (4.47 BW), peak vGRF of BBM-I slightly increased by 0.22% in the second cycle (4.48 BW), by 1.57%

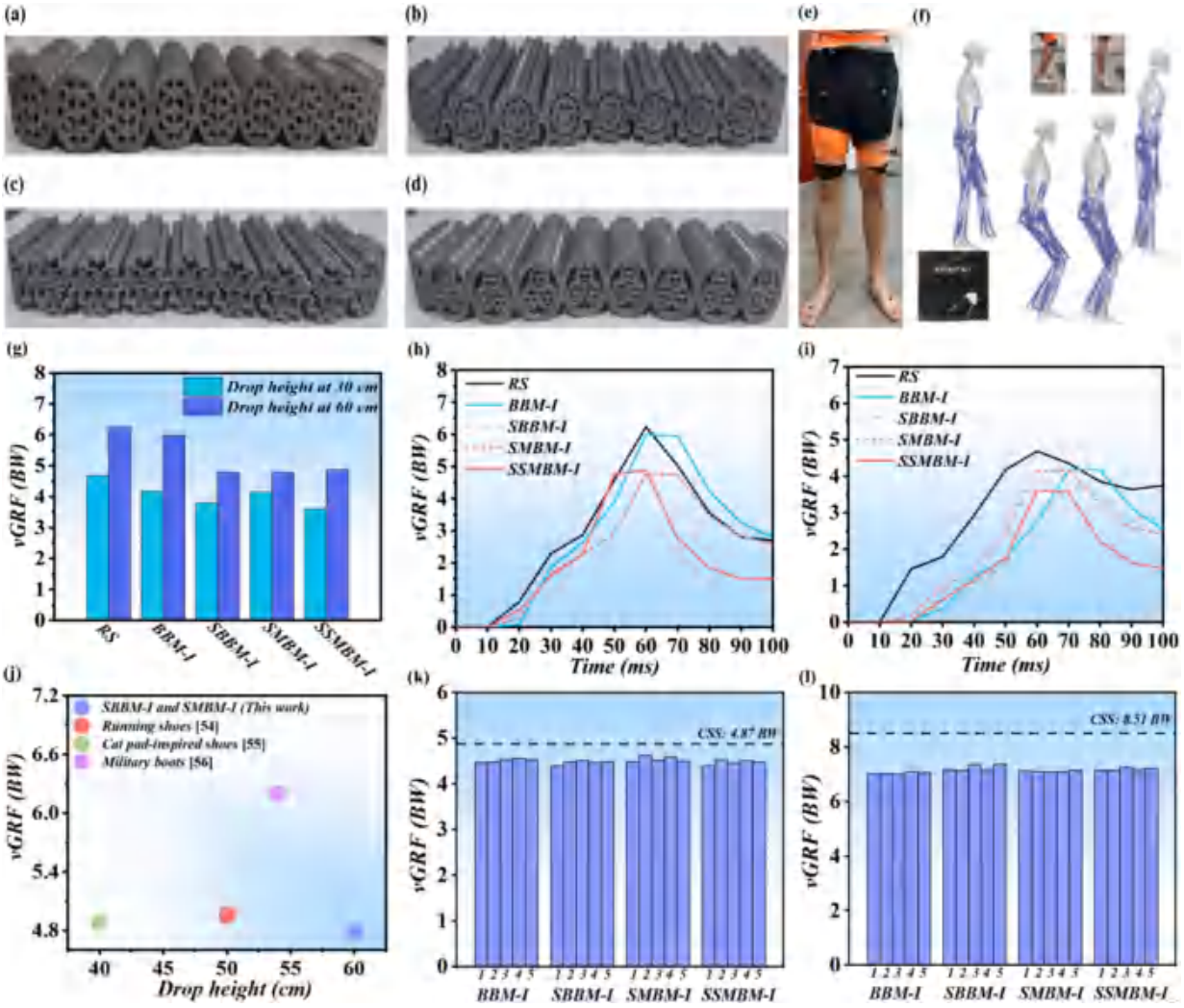

Fig. 7. Application demonstration of bio-inspired multifunctional insole on sports cushioning. (a) BBM-I. (b) SBBM-I. (c) SMBM-I. (d) SSMBM-I. (e) Location of reflective markers for motion analysis. (f) Schematic diagram of drop jump test. (g) Peak vGRF data of different insoles in drop jump test. (h) vGRF curve of different insoles at a drop height of 30 cm. (i) vGRF curve of different insoles at a drop height of 60 cm. (j) Peak vGRF data of insoles in this work and comparative data in previous studies. (k) Peak vGRF data of insoles in cyclic drop jumps from 30 cm. (l) Peak vGRF data of insoles in cyclic drop jumps from 60 cm. RS: running shoes; BBM-I: bamboo bionic metamaterials insole; SBBM-I: S-shaped bamboo bionic metamaterials insole; SMBM-I: skeletal muscle bionic metamaterials insole; SSMBM-I: S-shaped skeletal muscle bionic metamaterials insole. 1: first cycle; 2: second cycle; 3: third cycle; 4: fourth cycle; 5: last cycle.

in the third cycle (4.54 BW), by 2.01% in the fourth cycle (4.56 BW), and by 1.34% in the last cycle (4.53 BW). For SBBM-I, the peak vGRF rose by only 1.82% in the second cycle (4.48 BW), 2.5% in the third cycle (4.51BW), 1.59% in the fourth cycle (4.47 BW), and 2.05% in the last cycle (4.49 BW), compared to the first cycle (4.4 BW). Relative to the first cycle (4.49 BW), the peak vGRF of SMBM-I gradually increased by 2.9% in the second cycle (4.62 BW), 0.67% in the third cycle (4.52 BW), 2.23% in the fourth cycle (4.59 BW), and 0.22% in the last cycle (4.5 BW). For SSMBM-I, the peak vGRF slightly rose by 3.18% in the second cycle (4.54 BW), 1.36% in the third cycle (4.46 BW), 2.5% in the fourth cycle (4.51 BW), and 1.82% in the last cycle (4.48 BW), compared to the first cycle (4.4 BW).

In cyclic drop jumps from 60 cm, each BMI still exhibited good repeatability of cushioning performance (Fig. 7l, Table S12). For BBM-I, the absolute variation of peak vGRF was only 0.29% in the second cycle (7.03 BW), 0.14% in the third cycle (7 BW), 1.28% in the fourth cycle (7.1 BW), and 0.86% in the last cycle (7.07 BW), compared to the first cycle (7.01 BW). Relative to the first cycle (7.17 BW), the absolute variation of peak vGRF for SBBM-I was merely 0.42% in the second cycle (7.14 BW), 2.51% in the third cycle (7.35 BW), 0.14% in the fourth cycle (7.18 BW), and 2.79% in the last cycle (7.37 BW). For SMBM-I, the absolute variation of peak vGRF was merely 0.42% in the second cycle (7.1 BW), 0.7% in the third cycle (7.08 BW), 0.56% in the fourth cycle (7.09 BW), and 0.14% in the last cycle (7.14 BW), compared to the first cycle (7.13 BW). Relative to the first cycle (7.14 BW), the absolute variation of peak vGRF for SSMBM-I was only 0% in the second cycle (7.14 BW), 1.54% in the third cycle (7.25 BW), 0.56% in the fourth cycle (7.18 BW), and 1.26% in the last cycle (7.23 BW). Notably, the results demonstrated that the peak vGRF of all BMIs was significantly smaller than the corresponding value of CSS in the cyclic DJ test, indicating that BMI was highly effective for sports cushioning during SSC.

To optimize and personalize the exercise load of athletes, i.e., exercise volume, exercise intensity, various instruments, such as motion analysis systems, force platforms, surface electromyography, inertial measurement unit, etc., were used in biomechanical measurement, which was expensive, uncomfortable, inconvenient, and time-consuming for real-time training monitoring. In contrast, flexible wearable devices were able to fit the skin or to integrate into sports equipment, which has good wearing comfort and measuring convenience. In this study, PCMD was introduced to BMI for sports monitoring of SSC with different transition times (T_t) between eccentric phase and concentric phase, such as fast SSC (T_t<250 ms) or slow SSC (T_t>250 ms).

Composed of MXene, CNC, and PVA, PCMD was green synthesized via one-pot synthesis. Due to its high conductivity, abundant surface functional group, and exceptional hydrophily, MXene, i.e., a novel two-dimensional layered nanomaterials, was selected to build the conductive path. However, the strong van der Waals (VDW) interaction of nano-sized MXene easily leads to the restacking and aggregation of MXene, which significantly harms the electrical stability and mechanical properties of the hydrogel. As a highly crystalline rod-like nanomaterial, MXene has an abundant hydrophilic hydroxyl group on its surface. Its hydrophilic hydroxyl group not only formed multitudinous hydrogen bonds with oxygen-containing groups, to enhance the uniform dispersion of MXene, but also prevented the aggregation of MXene and increased the conductivity and stress/strain sensitivity of the hydrogel. In addition, CNC was served as a rigid sub-network for hydrogel, which was highly cross-linked with flexible PVA to enhance the mechanical property. Subsequently, borax was introduced into the polymeric system. Tetrahedral borate ion ($B(OH)_4^-$) and hydroxyl group on the PVA molecular chain formed the dynamic covalent bond, to induce the formation of a secondary network of hydrogel, which further improved the conductivity and strain sensitivity.

Intermolecular interactions of PVA hydrogel, PCM hydrogel, and PCMD hydrogel were validated using a Fourier transform infrared (FTIR) spectrometer, respectively (Fig. 8b). For PVA hydrogel, a strong absorption peak at the wavenumber of 3286 cm^{-1} was attributed to the stretching vibration of hydroxyl (-OH) in the PVA chain and the formation of intermolecular hydrogen bonds. After introducing CNC and Maxene, the strong characteristic peak (-C=O) for PCMD hydrogel at the wavenumber of 1661 cm^{-1} demonstrated that a strong hydrogen bonding interaction existed among CNC, MXene, and PVA. Furthermore, a significant peak appeared at the wavenumber of 608 cm^{-1} for PCM hydrogel, due to the bending vibration of B-O-C, which proved the formation of a dynamic boronic ester bond. Fig. 8d displayed the C1s, O1s, and Ti2p in X-ray photoelectron spectroscopy (XPM) for PVA hydrogel, PCM hydrogel, and PCMD hydrogel. C1s spectrum was constituted by C-Ti(283.98 eV), C=O(288.48 eV), C-O(285.78 eV), and C-C(284.58 eV). Compared to PCM hydrogel, PCMD hydrogel showed an extra C-O-B characteristic peak, indicating the introduction of borate ions. In the O1s spectrum, the binding energy for the C-Ti-O bond, C-Ti-OH bond, and C-O-C bond was 530.18 eV, 531.68 eV, and 532.28 eV, respectively, while PCMD hydrogel has a B—O characteristic peak (533.48 eV). It is consistent with the outcome from FTIR. Similarly, it has been found that binding energy for the Ti—C $2p_{1/2}$ bond, Ti—O $2p_{3/2}$ bond, and Ti—C $2p_{3/2}$ bond was 460.68 eV, 456.68 eV, and 453.58 eV, respectively, which indicated that the MXene's structure had not been damaged during the formation of the molecular bond. The thermal behavior of hydrogel with different components was studied via thermogravimetric analysis (TGA) (Fig. 8c, Fig. S39). The result indicated that the PVA hydrogel experienced a rapid weight-loss process from 260 °C to 500 °C. Its rate of weight loss is 95%, which suggests that PVA hydrogel was almost completely degraded. The initial decomposition temperature of PCM hydrogel and PCMD hydrogel was raised from 260 °C to 300 °C, because hydrogen bonds have been formed among CNC, MXene, and PVA, which increased the thermal stability. Microstructure from the cross-section of freeze-dried hydrogel was observed using a scanning electron microscope (SEM) (Fig. 8e). Irregular macroporous strip structure was observed in PVA hydrogel. Due to hydrogen bonds among CNC, MXene, and PVA, a smaller aperture and a stronger interconnected conductive network were generated in PCM hydrogel. It not only enhances the mechanical property of PCM hydrogel but also provides more channels for fast transmission of conductive ions. The uniform distribution of Ti was observed in energy dispersive spectroscopy (EDS) (Fig. S40). Thus, CNC can be a green dispersant for MXene, which is vital to electrical conductivity and sensing performance for hydrogel. Before evaluating the capability of the PCMD hydrogel sensor in recognizing human motion intentions, its response characteristics were characterized (Fig. 8f). The results demonstrated that the sensor exhibited a highly discernible monotonic relationship between relative resistance and applied strain across the full 100% strain range. To further assess its stability and repeatability, long-term cyclic loading-unloading tests were performed on the PCMD hydrogel sensor. As shown in Fig. 8g, the resistance signal remained stable over more than 1500 cycles with no significant drift, indicating excellent cyclic stability and supporting its potential for long-term monitoring applications. In strain sensing property, PCMD possessed good repeatability on peak value and waveform of relative resistance ($\Delta R/R_0$), and precisely distinguished the large strain and small strain in the musculoskeletal system under various motions, such as wrist curl, elbow flexion, and finger flexion (Fig. 8h-j, Fig. S41–43). It proved that PCMD could be used to develop the piezoresistive sensor in BMI.

PCMD was assembled on the hindfoot area of the upper surface of the BMI, because the heel was one of the main concentration zones of plantar pressure during SSC (Fig. 9a). When compressive strain that resulted from the pressure of the hindfoot appeared, the corresponding magnitude of $\Delta R/R_0$ was synchronously output from BMI. Different locomotion could be identified based on unique peak values, signal frequency, and the waveform generated in the $\Delta R/R_0$-time curve. To measure the $\Delta R/R_0$ of the BMI in different types of SSC, heel-raising, stepping, and countermovement jump (CMJ) were performed to replicate the slow SSC, while DJ was also implemented to simulate the fast SSC. Due to the difference in contact time between the heel and the sensor, the peak value of the $\Delta R/R_0$-timecurve for stepping was approximately three times that of heel-raising, but the signal frequency of $\Delta R/R_0$ during heel-raising was higher than that of stepping (Fig. 9b-c). Besides, the more dramatic fluctuation occurred in the $\Delta R/R_0$-time curve generated by DJ, relative to the $\Delta R/R_0$ of CMJ, because of inconsistency in drop height and ground contact time (Fig. 9d-e). It has been concluded that the BMI was able to recognize different motions and different types of SSC, which have potential applications in exercise load monitoring in competitive sports. It can provide accurate information for coaches, sports analysts, and kinesiotherapists to adjust future training programs of athletes.

5. Conclusion

To conclude, the athlete always suffered from acute sports injury in the eccentric phase of SSC, when the sports-specific movement was performed. It not only ruined the physical health, sports-specific performance and sports career of athletes but also generated enormous economic loss to the national team and sports club. Thus, it is essential to develop sports equipment with high cushioning performance for the targeted protection of athletes. However, current sports equipment was unable to provide the targeted cushioning under the specific load that was generated in difficult sports-specific techniques owing to several shortcomings including a simple structure and single functionality. To the targeted cushioning for athletes, synthesizing the bionic feature of bamboo, skeletal muscle, and cuttlefish bone, the novel bio-inspired metamaterials with high energy absorbing capacity have been utilized to expand the structural design freedom of sports equipment in the study. The result proved that bio-inspired metamaterials exhibited excellent energy absorption (401.21 J). The BMI with both cushioning and sensing was developed by integrating bio-inspired metamaterials and the PCMD prepared using the one-pot method. It decreased the peak vertical ground reaction force to 76.6% of famous commercial running shoes, which can realize the targeted cushioning for athletes. Nevertheless, the piezoresistive sensor that is fixed on the BMI can monitor different locomotion from the fast SSC and the slow SSC, achieving the real-time monitoring of exercise load. In future, the BMI will fulfil a role in the field of competitive sports, including scientific training, injury prevention and equipment development. Besides, new generation smart sports equipment using shape memory materials will be fabricated to obtain the programmable and reconfigurable mechanical properties, which can perform high resilience or high cushioning behavior

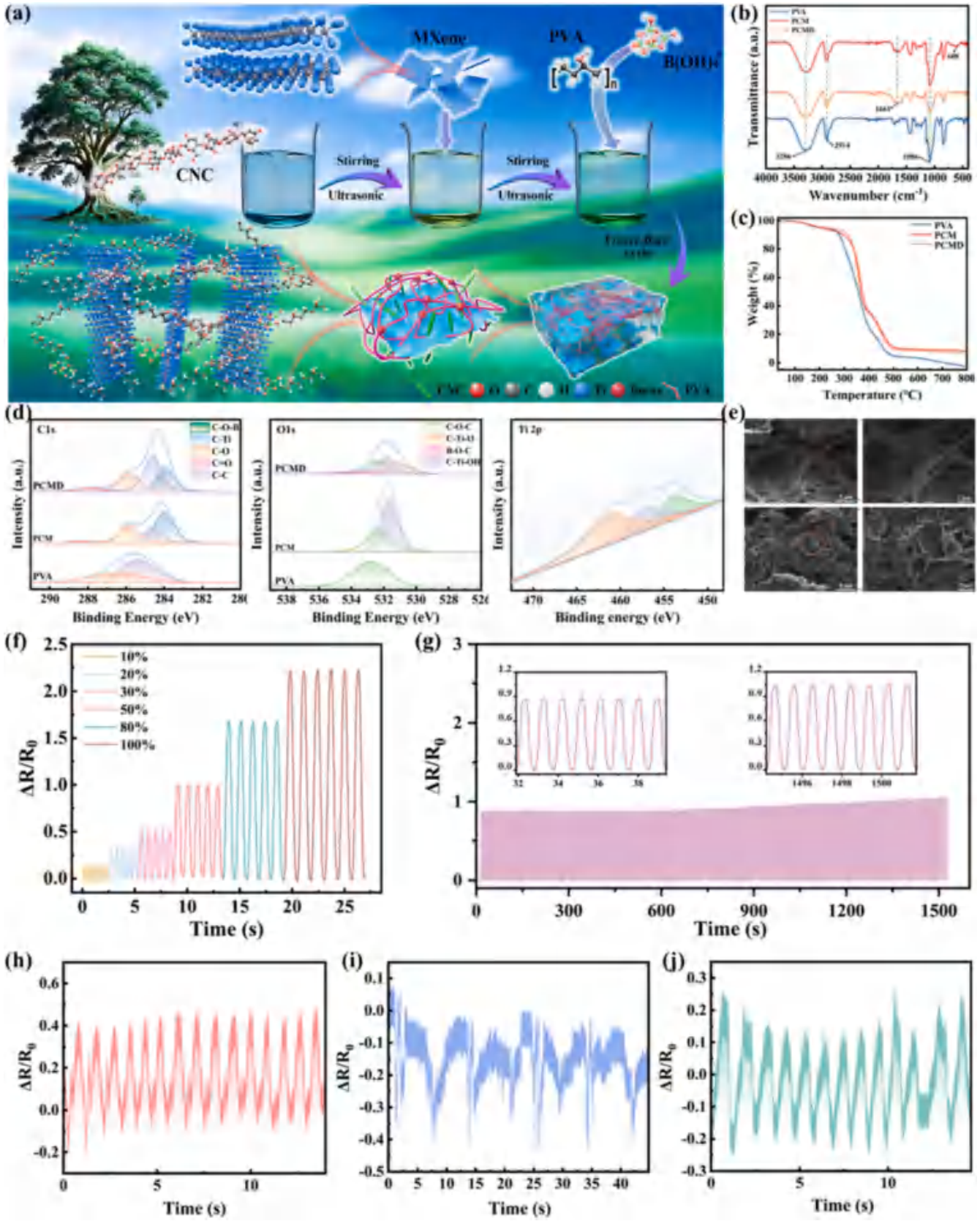

Fig. 8. Preparation and characterization of PCMD. (a) Preparation process for PCMD. (b) FTIR spectra. (c) TGA curve. (d) XPS spectra. (e) SEM micrograph. (f) Relative resistance change of the PCMD hydrogel sensor at 10%–100% strain. (g) Stability and repeatability tests of the sensor under 50% strain for 1500 cycles. (h) Relative resistance in wrist curl. (i) Relative resistance in elbow flexion. (j) Relative resistance in finger flexion.

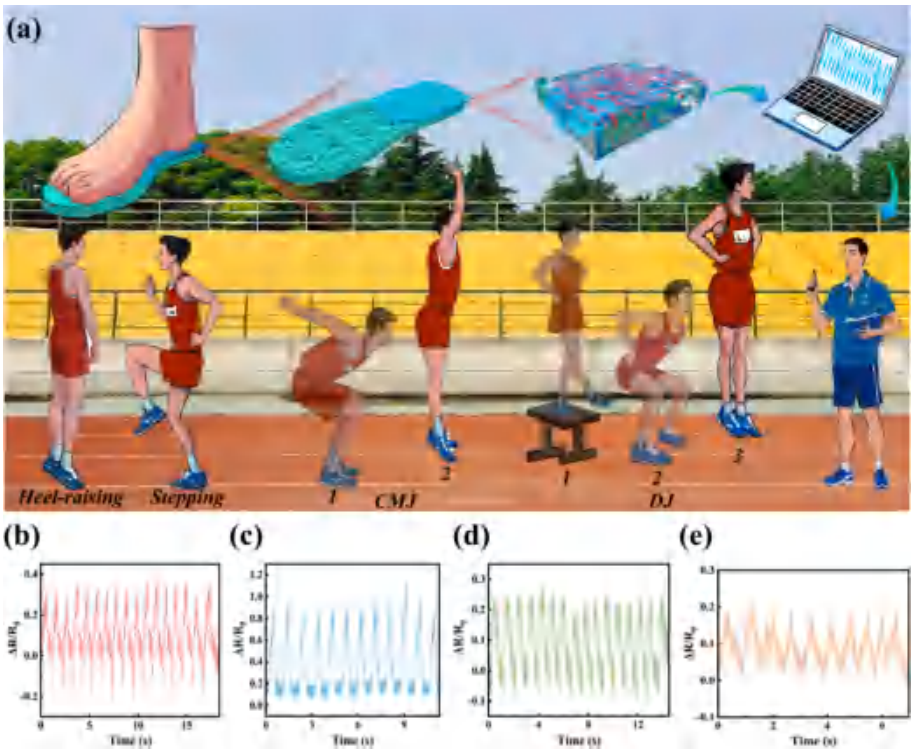

Fig. 9. Application demonstration of bio-inspired multifunctional insole on exercise load monitoring. (a) Preparation for piezoresistive sensor and different locomotion from fast SSC or slow SSC. (b) Relative resistance in heel-raising. (c) Relative resistance in stepping. (d) Relative resistance in DJ. (e) Relative resistance in CMJ.

according to the explosive power performance of athletes.

CRediT authorship contribution statement

Zehao Tong: Writing – review & editing, Writing – original draft, Software, Methodology, Investigation. **Cheng Lin:** Writing – review & editing, Writing – original draft, Visualization, Methodology. **Liwu Liu:** Writing – review & editing, Investigation, Funding acquisition. **Yanju Liu:** Supervision, Funding acquisition. **Jinsong Leng:** Supervision, Funding acquisition.

Declaration of competing interest

The authors declare that they have no known competing financial interests or personal relationships that could have appeared to influence the work reported in this paper.

Acknowledgements

The authors gratefully acknowledge the financial support provided by the National Key R&D Program of China (2022YFB3805700).

Appendix A. Supplementary data

Supplementary data to this article can be found online at https://doi.org/10.1016/j.cej.2026.174178.

Data availability

Data will be made available on request.

References

[1] Z.G. Nicolaou, A.E. Motter, Mechanical metamaterials with negative compressibility transitions, Nat. Mater. 11 (7) (2012) 608–613, https://doi.org/10.1038/nmat3331.
[2] X. Tan, Y. Li, L. Wang, K. Yao, Q. Ji, B. Wang, et al., Bioinspired flexible and programmable negative stiffness mechanical metamaterials, Adv. Intell. Syst. 5 (6) (2023) 2200400, https://doi.org/10.1002/aisy.202200400.
[3] W. Liu, S. Janbaz, D. Dykstra, B. Ennis, C. Coulais, Harnessing plasticity in sequential metamaterials for ideal shock absorption, Nature 634 (8035) (2024) 842–847, https://doi.org/10.1038/s41586-024-08037-0.
[4] L. Zhang, F. Pan, Y. Ma, K. Yang, S. Guo, Y. Chen, Bistable reconfigurable origami metamaterials with high load-bearing and low state-switching forces, Extreme Mech. Lett. 63 (2023) 102064, https://doi.org/10.1016/j.eml.2023.102064.
[5] X. Guo, X. Ni, J. Li, H. Zhang, F. Zhang, H. Yu, et al., Designing mechanical metamaterials with kirigami-inspired, hierarchical constructions for giant positive and negative thermal expansion, Adv. Mater. 33 (3) (2021) e2004919, https://doi.org/10.1002/adma.202004919.
[6] L.R. Meza, S. Das, J.R. Greer, Strong, lightweight, and recoverable three-dimensional ceramic nanolattices, Science 345 (6202) (2014) 1322–1326, https://doi.org/10.1126/science.1255908.
[7] C. Lin, M. Yang, F. Zhang, Y. Liu, J. Leng, Stimuli-responsive smart materials for biomedical applications, Mater. Sci. Eng. R. Rep. 167 (2026) 101126, https://doi.org/10.1016/j.mser.2025.101126.
[8] X. Tan, S. Chen, S. Zhu, B. Wang, P. Xu, K. Yao, et al., Reusable metamaterial via inelastic instability for energy absorption, Int. J. Mech. Sci. 155 (2019) 509–517, https://doi.org/10.1016/j.ijmecsci.2019.02.011.
[9] K. Fu, Z. Zhao, L. Jin, Granular metamaterials: programmable granular metamaterials for reusable energy absorption, Adv. Funct. Mater. 29 (32) (2019) 1970223, https://doi.org/10.1002/adfm.201970223.
[10] S. Yuan, C.K. Chua, K. Zhou, 3D-printed mechanical metamaterials with high energy absorption, Adv. Mater. Technol. 4 (3) (2019) 1800419, https://doi.org/10.1002/admt.201800419.
[11] E. Etemadi, A.M.M. Zamani, F. Scarpa, M. Zeeshan, M. Hosseinabadi, H. Hu, Modified re-entrant auxetic metamaterials with energy absorption enhancement, Mater. Today Commun. 38 (2024) 108079, https://doi.org/10.1016/j.mtcomm.2024.108079.
[12] H. Fan, Y. Tian, L. Yang, D. Hu, P. Liu, Multistable mechanical metamaterials with highly tunable strength and energy absorption performance, Mech. Adv. Mater. Struct. 29 (11) (2022) 1637–1649, https://doi.org/10.1080/15376494.2020.1834653.
[13] C.L. Yang, X.Z. Xin, W.J. Zhao, C. Lin, L.W. Liu, Y.J. Liu, et al., Highly programmable 4D printed multi-shape gradient metamaterials and multifunctional

devices, Int. J. Extreme Manuf. 7 (5) (2025) 055504, https://doi.org/10.1088/2631-7990/add8ca.
[14] R. Hamzehei, A. Serjouei, N. Wu, A. Zolfagharian, M. Bodaghi, 4D metamaterials with zero Poisson's ratio, shape recovery, and energy absorption features, Adv. Eng. Mater. 24 (9) (2022) 2200656, https://doi.org/10.1002/adem.202200656.
[15] P. Wang, F. Yang, B. Zheng, P. Li, R. Wang, Y. Li, et al., Breaking the tradeoffs between different mechanical properties in bioinspired hierarchical lattice metamaterials, Adv. Funct. Mater. 33 (45) (2023) 2305978, https://doi.org/10.1002/adfm.202305978.
[16] R. Hamzehei, M. Bodaghi, J.A. Iglesias Martinez, Q. Ji, G. Ulliac, M. Kadic, et al., Parrot beak-inspired metamaterials with friction and interlocking mechanisms 3D/4D printed in micro and macro scales for supreme energy absorption/dissipation, Adv. Eng. Mater. 25 (11) (2023) 2201842, https://doi.org/10.1002/adem.202201842.
[17] W. Zhao, C. Yue, L. Liu, J. Leng, Y. Liu, Mechanical behavior analyses of 4D printed metamaterials structures with excellent energy absorption ability, Compos. Struct. 304 (2023) 116360, https://doi.org/10.1016/j.compstruct.2022.116360.
[18] A. Serjouei, A. Yousefi, A. Jenaki, M. Bodaghi, M. Mehrpouya, 4D printed shape memory sandwich structures: experimental analysis and numerical modeling, Smart Mater. Struct. 31 (5) (2022) 055014, https://doi.org/10.1088/1361-665X/ac60b5.
[19] S.A.S.A. Saufi, M.Y.M. Zuhri, M.L. Dezaki, S.M. Sapuan, R.A. Ilyas, A. As'arry, et al., Compression behaviour of bio-inspired honeycomb reinforced starfish shape structures using 3D printing technology, Polymers 13 (24) (2021), https://doi.org/10.3390/polym13244388.
[20] J.H. Zhao, M. Li, J.W. Chen, W.W. Gao, H. Bai, Energy-absorbing porous materials: bioinspired architecture and fabrication, Nano Res. 16 (12) (2023) 13322–13334, https://doi.org/10.1007/s12274-023-6223-8.
[21] M. Zou, S. Xu, C. Wei, H. Wang, Z. Liu, A bionic method for the crashworthiness design of thin-walled structures inspired by bamboo, Thin-Walled Struct. 101 (2016) 222–230, https://doi.org/10.1016/j.tws.2015.12.023.
[22] S.H. Siddique, P.J. Hazell, H. Wang, J.P. Escobedo, A.A.H. Ameri, Lessons from nature: 3D printed bio-inspired porous structures for impact energy absorption – a review, Addit. Manuf. 58 (2022) 103051, https://doi.org/10.1016/j.addma.2022.103051.
[23] B.C. Chen, M. Zou, G.M. Liu, J.F. Song, H.X. Wang, Experimental study on energy absorption of bionic tubes inspired by bamboo structures under axial crushing, Int. J. Impact Eng. 115 (2018) 48–57, https://doi.org/10.1016/j.ijimpeng.2018.01.005.
[24] H.H. Tsang, K.M. Tse, K.Y. Chan, G. Lu, A.K.T. Lau, Energy absorption of muscle-inspired hierarchical structure: experimental investigation, Compos. Struct. 226 (2019) 111250, https://doi.org/10.1016/j.compstruct.2019.111250.
[25] H.H. Tsang, S. Raza, Impact energy absorption of bio-inspired tubular sections with structural hierarchy, Compos. Struct. 195 (2018) 199–210, https://doi.org/10.1016/j.compstruct.2018.04.057.
[26] L. Chen, C.Y. Cui, X. Cui, J. Lu, Cuttlebone-inspired honeycomb structure realizing good out-of-plane compressive performances validated by DLP additive manufacturing, Thin Wall Struct. 198 (2024) 11768, https://doi.org/10.1016/j.tws.2024.111768.
[27] Y. Wang, X. Chen, Y. Sun, J. Zhang, J. Hu, L. Bai, Full-band vibration isolation and energy absorption via cuttlebone-inspired lattice structures, Int. J. Mech. Sci. 274 (2024) 109283, https://doi.org/10.1016/j.ijmecsci.2024.109283.
[28] F. Wu, B.-H. Sun, Study on functional mechanical performance of array structures inspired by cuttlebone, J. Mech. Behav. Biomed. Mater. 136 (2022) 105459, https://doi.org/10.1016/j.jmbbm.2022.105459.
[29] C.Y. Cui, L. Chen, S. Feng, X.G. Cui, J.Z. Lu, Compressive resistance of the bio-inspired cuttlebone-like sandwich structure under quasi-static load, Int. J. Mech. Sci. 248 (2023) 108222, https://doi.org/10.1016/j.ijmecsci.2023.108222.
[30] A. Mao, N. Zhao, Y. Liang, H. Bai, Mechanically efficient cellular materials inspired bycuttlebone, Adv. Mater. 33 (15) (2021) 2007348, https://doi.org/10.1002/adma.202007348.
[31] F. Wen, Y. Qian, Y. Gao, X. Zhou, L. Lyu, 3D woven tubular composites with bamboo-structures for enhanced energy absorption: designing, manufacturing and performance analysis, Polym. Compos. 45 (9) (2024) 8282–8295, https://doi.org/10.1002/pc.28340.
[32] M.J. Prajapati, A. Kumar, S.-C. Lin, J.-Y. Jeng, Closed-cell metamaterial composites 3D printed with hybrid FFF process for tunable mechanical and functional properties, Thin-Walled Struct. 192 (2023) 111168, https://doi.org/10.1016/j.tws.2023.111168.
[33] B. Yang, W. Chen, R. Xin, X. Zhou, D. Tan, C. Ding, et al., Pomelo peel-inspired 3D-printed porous structure for efficient absorption of compressive strain energy, J. Bionic Eng. 19 (2) (2022) 448–457, https://doi.org/10.1007/s42235-021-00145-1.
[34] H. Yin, Y. Xiao, G. Wen, N. Gan, C. Chen, J. Dai, Multi-objective robust optimization of foam-filled bionic thin-walled structures, Thin-Walled Struct. 109 (2016) 332–343, https://doi.org/10.1016/j.tws.2016.10.011.
[35] W. Xu, C. Wang, B. Liu, S. Jia, Crushing responses and energy absorption of bionic inspired corrugated honeycombs, Int. J. Impact Eng. 179 (2023) 104641, https://doi.org/10.1016/j.ijimpeng.2023.104641.
[36] J. Fu, Q. Liu, K. Liufu, Y. Deng, J. Fang, Q. Li, Design of bionic-bamboo thin-walled structures for energy absorption, Thin-Walled Struct. 135 (2019) 400–413, https://doi.org/10.1016/j.tws.2018.10.003.
[37] B. Zhou, H. Zhang, S. Han, X. Ji, Crashworthiness analysis and optimization of a novel thin-walled multi-cell structure inspired by bamboo, Structures 59 (2024) 105827, https://doi.org/10.1016/j.istruc.2023.105827.
[38] Z. Zhuang, Z. Qian, X. Wang, X. Xu, B. Chen, G. Song, et al., Bioinspired structural composite flexible material with high cushion performance, Adv. Sci. 11 (5) (2024) 2304947, https://doi.org/10.1002/advs.202304947.
[39] F. Shen, S. Yuan, Y. Guo, B. Zhao, J. Bai, M. Qwamizadeh, et al., Energy absorption of thermoplastic polyurethane lattice structures via 3D printing: modeling and prediction, Int. J. Appl. Mech. 08 (07) (2016) 1640006, https://doi.org/10.1142/S1758825116400068.
[40] T. Yu, P. Xue, Introduction to Engineering Plasticity, Elsevier, Amsterdam, 2022.
[41] F. Huang, X. Zhou, D. Zhou, Y. Tao, Crashworthiness analysis of bio-inspired hierarchical circular tube under axial crushing, J. Mater. Sci. 58 (1) (2023) 101–123, https://doi.org/10.1007/s10853-022-07982-3.
[42] L. Yuan, D. Gu, X. Liu, K. Shi, K. Lin, H. Liu, et al., Design and additive manufacturing of bionic hybrid structure inspired by cuttlebone to achieve superior mechanical properties and shape memory function, Int. J. Extreme Manuf. 6 (5) (2024) 055001, https://doi.org/10.1088/2631-7990/ad5084.
[43] B. Van Hooren, J. Zolotarjova, The difference between countermovement and squat jump performances: a review of underlying mechanisms with practical applications, J. Strength Cond. Res. 31 (7) (2017), https://doi.org/10.1519/JSC.0000000000001913.
[44] L.I. Wang, H.T. Peng, Biomechanical comparisons of single- and double-legged drop jumps with changes in drop height, Int. J. Sports Med. 35 (6) (2014) 522–527, https://doi.org/10.1055/s-0033-1345133.
[45] W.J. Markwick, S.P. Bird, J.J. Tufano, L.B. Seitz, G.G. Haff, The intraday reliability of the Reactive Strength Index calculated from a drop jump in professional men's basketball, Int. J. Sports Physiol. Perform. 10 (4) (2015) 482–488, https://doi.org/10.1123/ijspp.2014-0265.
[46] D. Boullosa, C.C.C. Abad, V.P. Reis, V. Fernandes, C. Castilho, L. Candido, et al., Effects of drop jumps on 1000-m performance time and pacing in elite male and female endurance runners, Int. J. Sports Physiol. Perform. 15 (7) (2020) 1043–1046, https://doi.org/10.1123/ijspp.2019-0585.
[47] J.A. Washif, L.Y. Kok, The reactive bounding coefficient as a measure of horizontal reactive strength to evaluate stretch-shortening cycle performance in sprinters, J. Hum. Kinet. 73 (2020) 45–55, https://doi.org/10.2478/hukin-2020-0003.
[48] M.J. Barr, V.W. Nolte, Which measure of drop jump performance best predicts sprinting speed? J. Strength Cond. Res. 25 (7) (2011) 1976–1982, https://doi.org/10.1519/JSC.0b013e3181e4f7ba.
[49] R. Ramirez-Campillo, C. Alvarez, F. Garcia-Pinillos, J. Sanchez-Sanchez, J. Yanci, D. Castillo, et al., Optimal reactive strength index: is it an accurate variable to optimize plyometric training effects on measures of physical fitness in young soccer players? J. Strength Cond. Res. 32 (4) (2018) 885–893, https://doi.org/10.1519/JSC.0000000000002467.
[50] J. Plesa, Z. Kozinc, D. Smajla, N. Sarabon, The association between reactive strength index and reactive strength index modified with approach jump performance, PLoS One 17 (2) (2022) e0264144, https://doi.org/10.1371/journal.pone.0264144.
[51] J. Jang, J.R. Franz, B.G. Pietrosimone, E.A. Wikstrom, Muscle contributions to reduced ankle joint contact force during drop vertical jumps in patients with chronic ankle instability, J. Biomech. 163 (2024) 111926, https://doi.org/10.1016/j.jbiomech.2024.111926.
[52] L. Chen, Z. Jiang, C. Yang, R. Cheng, S. Zheng, J. Qian, Effect of different landing actions on knee joint biomechanics of female college athletes: based on opensim simulation, Front. Bioeng. Biotechnol. 10 (2022) 899799, https://doi.org/10.3389/fbioe.2022.899799.
[53] C.Y. Cui, L. Chen, S. Feng, X. Cui, J. Lu, Novel cuttlebone-inspired hierarchical bionic structure enabled high energy absorption, Thin-Walled Struct. 186 (2023) 110693, https://doi.org/10.1016/j.tws.2023.110693.
[54] I.L. Wang, J.-J. Gao, L.-I. Wang, K.-K. Zhang, Effects of shoe weight on landing impact and side-to-side asymmetry, PLoS One 16 (8) (2021) e0256061, https://doi.org/10.1371/journal.pone.0256061.
[55] Y.L. Xiao, D.Y. Hu, Z.Q. Zhang, B.Q. Pei, X.Q. Wu, P. Lin, A 3D-printed sole design bio-inspired by cat paw pad and triply periodic minimal surface for improving paratrooper landing protection, Polymers-Basel 14 (16) (2022) 3270, https://doi.org/10.3390/polym14163270.
[56] S. Aziz, K.B. Gan, A.S. Rambely, K. Gopal, M.S. Ariffin, N. Shattar, Relationship between angle and peak vertical ground reaction force estimation in parachute landing fall among army parachutists using mathematical modelling, Alex. Eng. J. 61 (7) (2022) 5413–5426, https://doi.org/10.1016/j.aej.2021.11.005.